Nucleation rate of carbonaceous nanoparticles by n-heptane pyrolysis at high pressure and temperature via molecular dynamics simulations

Fakharnezhad, Arash; Saad, Dimitri M.; Kelesidis, Georgios A.; Goudeli, Eirini

DOI
10.1080/02786826.2025.2480625

Publication date
2025

Document Version
Final published version

Published in
Aerosol Science and Technology

Aerosol Science and Technology

ISSN: (Print) (Online) Journal homepage: www.tandfonline.com/journals/uast20

Nucleation rate of carbonaceous nanoparticles by n-heptane pyrolysis at high pressure and temperature via molecular dynamics simulations

Arash Fakharnezhad, Dimitri M. Saad, Georgios A. Kelesidis & Eirini Goudeli

To cite this article: Arash Fakharnezhad, Dimitri M. Saad, Georgios A. Kelesidis & Eirini Goudeli (03 Apr 2025): Nucleation rate of carbonaceous nanoparticles by n-heptane pyrolysis at high pressure and temperature via molecular dynamics simulations, Aerosol Science and Technology, DOI: 10.1080/02786826.2025.2480625

To link to this article: https://doi.org/10.1080/02786826.2025.2480625

AEROSOL SCIENCE AND TECHNOLOGY
https://doi.org/10.1080/02786826.2025.2480625

Nucleation rate of carbonaceous nanoparticles by n-heptane pyrolysis at high pressure and temperature via molecular dynamics simulations

Arash Fakharnezhad[a], Dimitri M. Saad[b], Georgios A. Kelesidis[c,d], and Eirini Goudeli[a]

[a]Department of Chemical Engineering, The University of Melbourne, Parkville, Melbourne Victoria, Australia; [b]Department of Energy Science and Engineering, Stanford University, Stanford, California, USA; [c]Faculty of Aerospace Engineering, Delft University of Technology, Delft, The Netherlands; [d]Nanoscience and Advanced Materials Center (NAMC), Environmental and Occupational Health Science Institute, School of Public Health, Rutgers, The State University of New Jersey, Piscataway, New Jersey, USA

ABSTRACT

Chemical nucleation of carbonaceous nanoparticles is investigated during pyrolysis of n-heptane at high temperature (2200–2600 K) by reactive molecular dynamics (MD) simulations. The MD-derived n-heptane consumption rate is in agreement with kinetic modeling, validating the present work at high temperature and high fuel concentration conditions. The critical nucleus size is quantified by the free formation energy at 2200–2600 K for n-heptane concentrations ranging from 3×10^{20}–9×10^{20} #/cm^3. Increasing temperature leads to smaller critical size, starting from 59 ± 7 carbon atoms at 2200 K that decreases down to 33 ± 3 carbon atoms at 2600 K, while the fuel concentration hardly affects the critical nucleus size. The onset time of nucleation decreases exponentially with temperature, consistent with previous shock tube pyrolysis experiments. The nucleation rate is obtained by the rate of formation of critical and supercritical hydrocarbon molecules. An Arrhenius-type relationship between the nucleation rate and the process temperature is proposed, exhibiting a first-order dependency to the initial fuel concentration. The number density of carbon nuclei derived by this nucleation rate is four to five orders of magnitude higher than that obtained by kinetic models for soot nucleation by reactive polyaromatic hydrocarbon (PAH) dimerization. The present MD-derived nucleation rate provides a computationally efficient pathway to model carbonaceous nanoparticle formation dynamics without relying on individual chemical reaction rate constants or on computationally expensive PAH-based models.

GRAPHICAL ABSTRACT

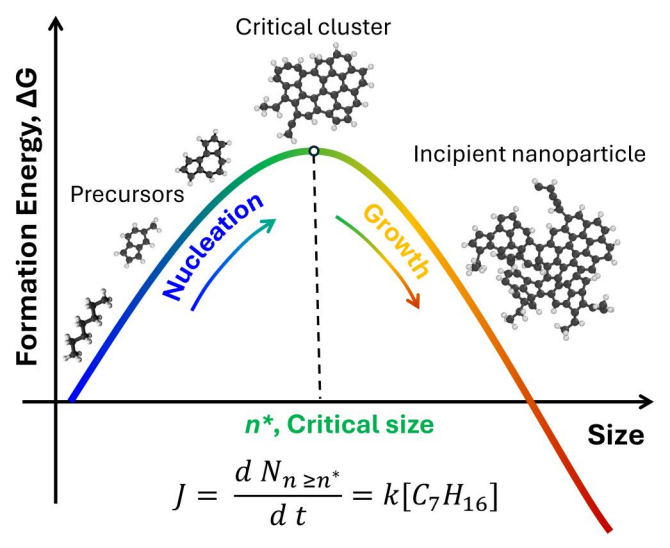

ARTICLE HISTORY
Received 29 November 2024
Accepted 3 March 2025

EDITOR
Jason Olfert

CONTACT Eirini Goudeli eirini.goudeli@unimelb.edu.au Department of Chemical Engineering, The University of Melbourne, Parkville, Melbourne VIC 3010, Australia.

Supplemental data for this article can be accessed online at https://doi.org/10.1080/02786826.2025.2480625.

1. Introduction

Carbon black is the largest nanomaterial produced industrially today, primarily through the combustion of residual fuel oil (International Carbon Black Association 2016). These nanoparticles are used in a wide range of applications, including inks, tires, and paints, contributing to a $16 billion industry worldwide. Recently, carbon black has also been incorporated into lithium-ion batteries (Hu, Zhong, and Yan 2021) and supercapacitors (Ma et al. 2021) to meet the growing energy demands of society. In contrast, soot, a by-product of fossil-fuel combustion, has been at the forefront of research for several decades due to its adverse health effects (Jerrett et al. 2013) and negative impact on the environment and Earth's albedo (Bond et al. 2013). The large-scale transition toward net-zero emission technologies within the next 40 years, provided it is viable from technical, economic and social standpoint, remains a challenging undertaking (Smith et al. 2019). Therefore, research on combustion chemistry and a more systematic understanding of carbon-based nanoparticle formation are crucial not only for better product design but also for the development of cleaner combustion technologies and will play a pivotal role on this protracted transition (Kohse-Höinghaus 2020). The complexity in modeling carbonaceous nanoparticle formation, especially during nucleation, remains a significant challenge. Despite the low soot yield of nucleation compared to surface growth (Harris and Weiner 1985), it largely affects particle size distribution (Veshkini et al. 2016), and chemical composition quantified by its mass spectra (Raj et al. 2010), all of which are critical for determining end-product properties and meeting emission regulations (Kholghy et al. 2019).

Polyaromatic hydrocarbons (PAHs) and, potentially, their resonance-stabilized radicals (Gentile et al. 2020; Johansson et al. 2018), are the primary precursors of soot nucleation, a premise supported by recent theoretical calculations (Frenklach 2002; Miller 2005), mass spectroscopy (Johansson et al. 2018), and atomic force microscopy imaging (Schulz et al. 2019). However, owing to the inherent challenges in capturing soot nucleation experimentally, the exact mechanism by which PAHs contribute to soot nucleation remains unclear (Wang 2011). In this regard, PAH dimerization is routinely applied as the main soot nucleation mechanism in soot models.

Models for soot nucleation can be classified (Kennedy 1997) into semi-empirical and detailed kinetic ones. Semi-empirical models are obtained by fitting simplified theoretical nucleation rates to soot volume fraction data. Such models (Brookes and Moss 1999) are widely used in mathematical frameworks for practical flame (Li et al. 2023) and engine modeling (Stiesch 2003). The preference for employing these semi-empirical models is primarily rooted in their ability to offer an optimal balance between modeling precision and computational efficiency (Kleiveland 2005). Soot nucleation correlations used in these models directly relate the nucleation rate either to the parent hydrocarbon fuel (Gilyazetdinov 1972) or to intermediate species concentrations (Leung, Lindstedt, and Jones 1991; Moss, Stewart, and Young 1995), simplifying the complex chemistry of soot nucleation (Tanelli and Maranta 2015). Experimental evidence shows soot nucleation is primarily driven by key intermediate species, such as acetylene (Leung, Lindstedt, and Jones 1991) or benzene (Lindstedt 1994), whose concentration is indicative of the nucleation region during combustion of light ethylene, methane and heavy propane fuels (Lindstedt 1994), respectively. However, semi-empirical models are often valid only for the narrow range of combustion conditions used in the fitted experimental data set. So, quantitative, mechanistic models for soot nucleation are essential to design cleaner combustion engines.

The most widely accepted detailed kinetic model, proposed by Frenklach and Wang (1994), provides a comprehensive chemical reaction framework for PAH formation, as well as for nucleation and growth of soot. Soot nucleation was assumed to occur through dimerization of PAHs (Frenklach and Wang 1994). One widely studied hypothesis to describe transition from PAH molecules to solid-like carbonaceous particles is the dimerization of PAHs, especially, pyrene, held together irreversibly by physical van der Waals forces (Frenklach and Wang 1991; Schuetz and Frenklach 2002). The stability of such dimers at the high temperature environment of flames has been questioned (Mao, van Duin and Luo 2017; Sabbah et al. 2010) as larger PAHs, such as circumpyrene or circumcoronene, may be more likely to initiate physical nucleation due to their stronger physical interactions (Mao, van Duin, and Luo 2017). However, the role of large PAHs in nucleation is unclear, as their concentration decreases dramatically with increasing PAH size (Wang 2011). Additionally, soot particles are incepted at short residence times and reach their peak concentrations before medium-sized PAHs, such as coronene, appear (Siegmann, Sattler, and Siegmann 2002). Gleason et al. (2021) measured the number concentrations of soot and large aromatic structures

(up to six-rings) in counterflow diffusion flames by combined soot pyrometry and light scattering and compared them against a nucleation kinetic model by physical self-dimerization of different PAHs, revealing that only small aromatic structures (with one or two rings) can contribute to soot nucleation.

Nevertheless, the specific PAHs that contribute to soot nucleation and the underlying mechanism responsible for this transition are not fully understood (Wang 2011), as physical PAH dimerization cannot explain soot nucleation in flames above 1000 K (Sabbah et al. 2010). The weak bonding of PAH dimers leads to dissociation upon collisions with surrounding species, preventing their growth into larger soot particles. Thus, physical nucleation is less likely to occur at moderate temperatures (e.g., 1600 K) (Mao, van Duin, and Luo 2017). Recently, the role of chemical nucleation has been revisited, especially at high temperatures (D'Anna 2009; Frenklach and Mebel 2020; Johansson et al. 2018; Kholghy, Kelesidis and Pratsinis 2018; Kholghy et al. 2019; Mao, van Duin and Luo 2017). So, chemical and physical-chemical mechanisms for soot nucleation have been proposed based on experimental data (Johansson et al. 2018), density functional theory (DFT) (Martin et al. 2019), and molecular dynamics (MD) simulations (Martin, Salamanca, and Kraft 2022). Soot nanoparticles can be incepted by reactions between (a) aromatic aryl-linked hydrocarbons through the clustering of hydrocarbon radical chain reactions mechanism (Johansson et al. 2018); (b) aromatic rim-linked hydrocarbons involving localized π-radicals; (c) aromatic multicenter-linked hydrocarbons involving π-radicals; and (d) aromatic zig-zag-linked hydrocarbons involving diradicaloids (Martin, Salamanca, and Kraft 2022). Even though the kinetic constants for some of the above reactions have been computed (Menon et al. 2020), they have not been incorporated in detailed kinetic models for soot formation and lack quantitative validation with experimental data. To this end, Kholghy et al. (2019) and Kholghy, Kelesidis, and Pratsinis (2018) developed a semi-empirical kinetic model based on soot volume fraction measurements in a lean premixed "nucleation flame" (Desgroux et al. 2017), as well as in rich diffusion flames (Kholghy et al. 2019), showing that reactive dimerization of PAHs can limit the reversibility of soot nucleation. This highlights the need to account for soot chemical nucleation to derive robust nucleation rates. While PAH-based nucleation models have significantly advanced the understanding of soot nucleation, they require knowledge of detailed chemical reaction networks rendering them impractical to implement in large-scale complex systems. This highlights the need for alternative approaches, such as easy-to-use models that directly link nucleation to initial fuel concentration, bypassing intricate reaction networks that can be readily employed in practical applications like computational fluid dynamics simulations of combustion systems.

Here, chemical nucleation of carbonaceous nanoparticles during pyrolysis of n-heptane is investigated by reactive MD at high pressure and temperature for various initial fuel concentrations. The n-heptane consumption rate is validated with kinetic modeling, showing good agreement at the pressure and temperature conditions employed here. The critical nucleus size is determined by free formation energy calculations and a nucleation rate is obtained, for the first time to the best of our knowledge, without *a priori* assumptions of the chemical reaction network and associated rate constants, or of the nucleation mechanism. An expression of the nucleation rate is proposed as a function of temperature and initial fuel concentration and benchmarked with a semi-empirical kinetic model for reactive dimerization of PAHs (Kholghy, Kelesidis, and Pratsinis 2018).

2. Theory

2.1. Reactive MD

Reactive MD is used to simulate isothermal pyrolysis of n-heptane at 2200–2600 K, consistent with temperature measurements in gasoline direct injection engines (An et al. 2016; Figure 4b). One thousand n-heptane (C_7H_{16}) molecules are randomly distributed in a cubic simulation cell with initial fuel densities of $0.05-0.15\,g/cm^3$ using MAPS Scienomics 4.4 (Scienomics 2020). The length of the simulation domain spans from 103.5 to 149.5 Å, corresponding to initial fuel densities of 0.15 and $0.05\,g/cm^3$, respectively. The initial geometry of the n-heptane molecules was optimized in MAPS Scienomics at room temperature using the steepest descent algorithm, followed by system energy minimization. All MD simulations were performed with periodic boundary conditions in the NVT (constant number, volume, temperature) ensemble, using a ReaxFF forcefield for hydrocarbons (Ashraf and van Duin 2017) in LAMMPS (Plimpton 1995) with integration time step of 0.25 fs (Sharma et al. 2021), yielding consistent results with smaller time steps (Figure S1) and initially non-isothermal equilibration (FIgures S2 and S3). Furthermore, the potential energy of soot clusters made by n-heptane

pyrolysis using the employed ReaxFF (Ashraf and van Duin 2017) is in excellent agreement with that calculated by DFT (Schmalz et al. 2024), validating the present forcefield at the conditions of this study. However, accounting for π-radicals in resonance-stabilized systems would require the use of more chemically detailed methods, such as DFT, which can capture complex electronic interactions that are not adequately represented in the present ReaxFF (Chu, Wang, and Chen 2022). The chemical structures of the MD-obtained soot clusters are generated using ChemTraYzer (Döntgen et al. 2018).

2.2. Nucleation rate

The nucleation rate, J, is calculated by tracking the rate of change in the number density, $N_{n\geq\overline{n}}$, of clusters larger than a threshold size, $\overline{n}$ (Yasuoka and Matsumoto 1998):

$$J = \frac{dN_{n\geq\overline{n}}}{d\ t} \tag{1}$$

where t is the elapsed time. Equation (1) is applied in the nucleation-dominant region, where the rate of change in the number of clusters is constant (Yasuoka and Matsumoto 1998) and is defined for each threshold size, $\overline{n}$, as the region where the number concentration of that cluster size range spans from 20% to 80% of its maximum concentration (Halonen et al. 2021). When $\overline{n}$ exceeds the critical cluster size, steady-state nucleation is reached and the rate of change of the cluster concentration becomes independent of the cluster size (Halonen et al. 2021; Yasuoka and Matsumoto 1998).

2.3. Free formation energy soot clusters

The free energy of cluster formation, $\Delta G(n)$, representing the balance between the bulk and the cluster surface energy, is used to quantify the critical cluster size. The $\Delta G(n)$ is determined by monitoring the concentration, N_n, of soot clusters with size $i = 2, \ldots, n$, during steady-state nucleation (Halonen et al. 2021):

$$\Delta G(n) = -RT \sum_{i=2}^{n} \left[\ln N_n - \ln \left(N_{n-1} - \frac{J}{N_1 \beta_{n-1}} \right) \right] \tag{2}$$

where R is the gas constant, T is temperature, and N_1 and N_n are the averaged concentrations of monomers and clusters of size n during steady-state nucleation, respectively. By definition, the free formation energy of monomers, $\Delta G(1)$, is zero (Halonen et al. 2021). At steady-state, the nucleation rate, J, is given by the difference between the formation rate, $\beta_{n-1}N_1N_{n-1}$, and dissociation rate, $\alpha_n N_n$ (Halonen 2022; Halonen et al. 2021):

$$\beta_{n-1}N_1N_{n-1} - \alpha_n N_n = J \tag{3}$$

where β and α are collision and dissociation rate coefficients, respectively. The $\Delta G(n)$ (Equation (2)) is estimated assuming that soot cluster growth takes place only by addition of monomers (N_1) containing one to two carbon atoms. β is estimated by the kinetic gas theory (Halonen et al. 2021) as:

$$\beta = \gamma \sqrt{\frac{8\pi RT(n+1)}{nm}} (r_1 + r_n)^2 \tag{4}$$

where γ is the collision correction factor, m and r_1 are the monomer mass and radius, respectively, n is the number of monomers per cluster and r_n is the radius of a cluster with size n. For non-reactive systems (e.g., CO_2 [Halonen et al. 2021]), every collision is typically considered successful ($\gamma = 1$), however, when chemical reactions take place only a fraction of the collisions are reactive ($\gamma < 1$). Here, even though all CH_x and C_2H_x species contribute to the monomer concentration, N_1, for the calculation of $\Delta G(n)$ (Equation (2)), only radicals are assumed to lead to reactive collisions. So, the fraction of unsaturated hydrocarbons among the C_{1-2} species during steady-state nucleation (Figure S4) is used to determine γ in Equation (4). The impact of these assumptions is discussed in the online supplementary information.

2.4. Kinetic modeling of n-heptane pyrolysis and soot nucleation

The MD-derived dynamics of n-heptane pyrolysis are benchmarked against those obtained by a kinetic model using CHEMKIN PRO (Kee, Rupley, and Miller 1989). In particular, the pyrolysis of n-heptane with initial number density of 3×10^{20} #/cm^3 is simulated in a zero-dimensional batch reactor at constant temperature and volume of 2500 K and 1 cm^3, respectively, following closely the MD simulation conditions. The molar fraction and number density of n-heptane and its pyrolysis products are derived using the reaction mechanism of CaltechMech, validated for temperatures up to ~2300 K (Blanquart, Pepiot-Desjardins, and Pitsch 2009), with an integration time step of 0.1 ns. Soot nucleation during n-heptane pyrolysis is simulated using a semi-empirical model for reactive PAH dimerization (Kholghy, Kelesidis, and Pratsinis 2018), which models soot nucleation via reversible PAH clustering through van der Waals

forces, followed by irreversible chemical bond formation. This model integrates both physical and chemical pathways, allowing dimer stabilization even in hydrogen-deficient environments. The number density of soot nuclei is obtained from the molar fraction of the dimers formed between PAHs and contain 12–36 carbon atoms.

3. Results and discussion

3.1. Critical soot nucleus by reactive MD

Figure 1 shows snapshots of the formation of small linear and large polycyclic hydrocarbons and their subsequent growth to incipient carbonaceous nanoparticles during pyrolysis of n-heptane at 2500 K. Carbon–carbon bonds are depicted with black lines, while carbon–hydrogen bonds are omitted for clarity. At 1 ns (Figure 1a), cyclic molecules consisting of five- or six-member carbon rings are formed, followed by the formation of small polycyclic hydrocarbons, composed of up to four rings at 4 ns (Figure 1b). As these polycyclic hydrocarbons are subject to reactive collisions with linear or other small cyclic molecules, they grow into larger cyclic hydrocarbons at 8 ns (Figure 1c), and shortly after ($t = 12$ ns), to incipient soot nanoparticles (Figure 1d), upon condensation of small free radicals on their surface.

Initially ($t \leq 1$ ns), almost all n-heptane molecules dissociate, forming small mainly noncyclic aliphatic molecules (Figure S5a) and radicals, including C_2H_x and C_3H_x unsaturated hydrocarbons (Figure S5b), and a few cyclic structures containing one five- or six-member ring (Figure 1a: encircled molecules), consistent with pyrolysis products detected by ultraviolet photoionization mass spectrometry in n-heptane flames at 400 Pa and 780–1780 K (Yuan et al. 2011) and with previous ReaxFF simulations of n-heptane pyrolysis at 12–56 MPa and 1000–3000 K (Ding et al. 2013). These small reactive species, such as C_2H_2, increase the growth rate of molecules containing one ring to larger molecules composed of up to four rings (Figure 1b: encircled molecules) as evidenced by the increase in the formation rate of five- or six-member rings for $t \geq 1.7$ ns (Figure S6) consistent with PAH growth by Hydrogen Abstraction/Carbon Addition (Frenklach and Wang 1994).

Reactions of gaseous species on the surface of small polycyclic hydrocarbons (composed of up to four fused rings) lead to the formation of larger islands of polycyclic structures. For example, at 8 ns (Figure 1c) the encircled structures are composed of 7 (red), 11 (blue), and 12 rings (green). Finally, these structures grow further by surface reaction of small molecules (indicated by the drop in the number of C_2H_x and C_3H_x species in Figure S5) and by subsequent coagulation, resulting in the formation of incipient soot nanoparticles at 12 ns.

Figure 2 shows the temporal evolution of the number of clusters larger than a threshold number of carbon atoms, $\overline{n}$, during pyrolysis of n-heptane with initial concentration, N_0, of 6×10^{20} #/cm^3 at 2500 K. The evolution of the cluster count is shown for threshold sizes of $\overline{n} = 12$–42. Initially ($t = 0$), only n-heptane molecules ($n = 7$ carbon atoms) are present. So, the concentration of clusters with 12 carbon atoms or more is zero. As n-heptane decomposes, smaller reactive (Ding et al. 2013; Yuan et al. 2011) radicals are formed (Figure S5) that grow through clustering reactions into relatively large (≥15 carbon atoms) hydrocarbons at ~2 ns. For example, when a threshold size of $\overline{n} \geq 12$ is considered (dark blue line), the number of clusters consisting of 12 or more carbon atoms quickly increases from zero at $t = 0$ to a maximum of 117 at 7.3 ns, corresponding to 7.5% of the total number of hydrocarbon species at that time step. When the number of clusters spans between 20% and 80% (dot-broken lines) of their maximum concentration, the number of clusters increases linearly with time (slopes indicated by broken lines). There, the growth of those clusters takes place mainly by nucleation (Halonen et al. 2021). For example, for $\overline{n} \geq 12$, nucleation prevails between 1.8 and 6 ns. The limits of this regime are dictated by the threshold size, $\overline{n}$, as the number concentration of hydrocarbon species drops with increasing $\overline{n}$. So, a nucleation-dominant regime is defined (Figure 2: shaded region) based on the nucleus concentration of various threshold sizes, $\overline{n}$.

The initial time lag until the attainment of steady-state nucleation represents the time required for cluster formation and growth to a specific size (Diemand et al. 2013). For $t \geq 7.3$ ns and $\overline{n} \geq 12$, the cluster number concentration drops due to surface growth or cluster–cluster collisions. As $\overline{n}$ increases, formation of clusters of that size takes longer, while fewer such species form. After a certain threshold size is surpassed, the rate of change of the number of clusters is constant, indicated by the attainment of parallel slopes (Figure 2: $\overline{n} \geq 33$–42), corresponding to steady-state nucleation. These slopes quantify (Equation (1)) the nucleation rate, J, of clusters with at least $\overline{n}$ carbon atoms and serve as an indicator for the critical cluster size. So, the attainment of practically parallel slopes for $\overline{n} \geq 33$ ($t = 5$–8.2 ns), indicates that the critical

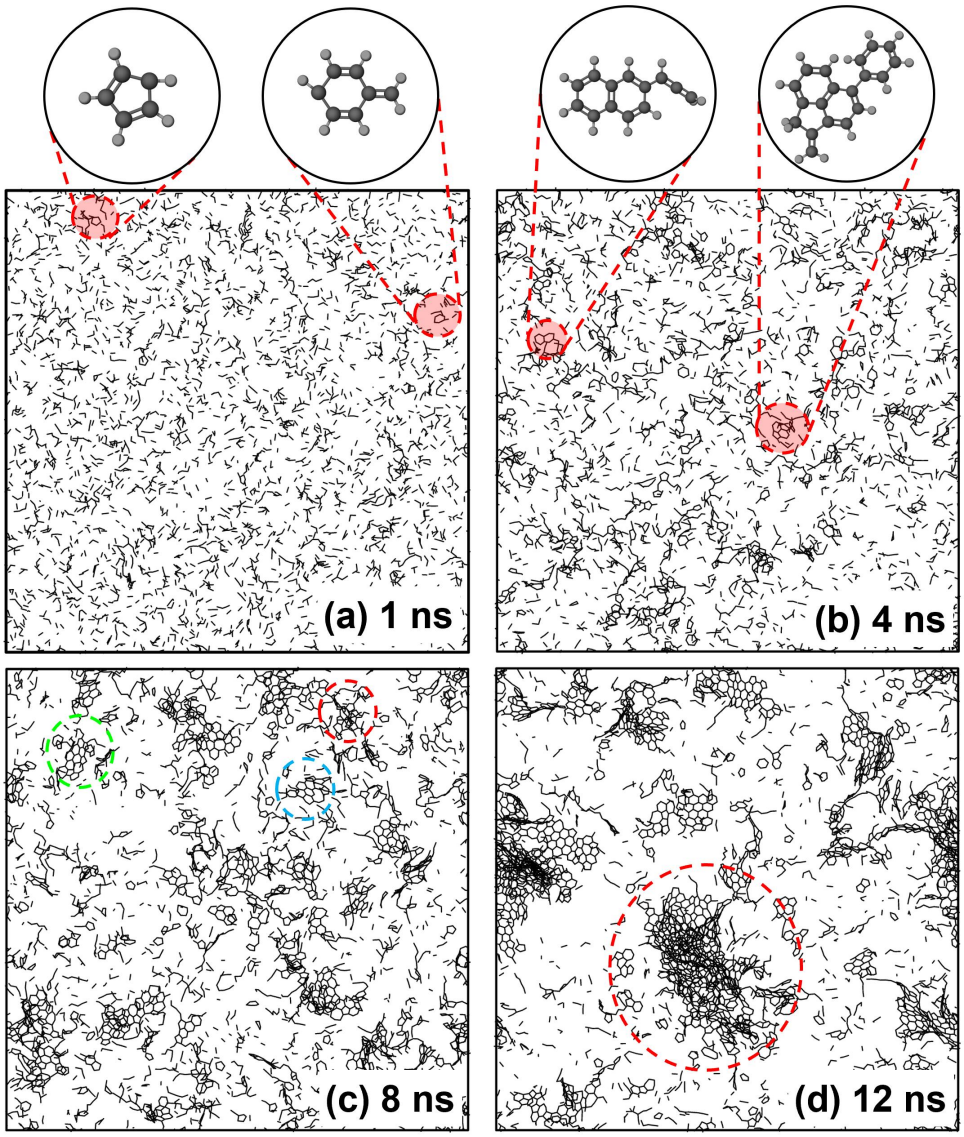

Figure 1. Snapshots of hydrocarbon molecules and their clusters derived by reactive MD for n-heptane (C_7H_{16}) pyrolysis at temperature $T = 2500$ K and residence times of (a) 1, (b) 4, (c) 8, and (d) 12 ns. The first cyclic structures ((a) encircled molecules) are formed, consisting primarily of five-membered rings rather than six-membered ones at 1 ns. At longer residence times ((b) $t = 4$ ns) more cyclic molecules are formed, which collide and react with each other, forming polycyclic hydrocarbons, with up to four rings (b) that grow further to large molecules with more than seven rings ((c) encircled molecules) and eventually to incipient soot nanoparticles ((d) encircled cluster).

cluster size has been surpassed and steady-state nucleation has been reached. As the cluster number concentrations approach their maximum, nuclei formation stops, followed by a decrease in cluster count due to surface growth or coagulation (Yasuoka and Matsumoto 1998).

Figure 3a shows the free formation energy, ΔG_n, (Equation (2)) of soot clusters formed during steady-state nucleation at 2200 (squares), 2300 (circles), 2400 (triangles), 2500 (inverse triangles), and 2600 K (diamonds) with $N_0 = 6 \times 10^{20}$ #/cm^3 using the J, N_1, and N_n, obtained during steady-state nucleation. Snapshots of randomly selected clusters with 10, 20, 39, 61, and 87 carbon atoms are shown as insets in Figure 3a at 2200 K. At all temperatures, small clusters are thermodynamically unstable forming and dissociating continuously. As the cluster size increases, ΔG_n passes through a maximum, corresponding to the critical soot nucleus, followed by a decrease in ΔG_n and subsequent growth of supercritical clusters. For example, at 2200 K (squares), clusters consisting of up to 52 carbon atoms are subcritical, as reflected by the increasing ΔG_n for $n \leq 52$. Once the free energy barrier of $\Delta G_n^* = 20.7$ kcal/mol is reached, critical clusters form. Notably, the free energy barrier decreases from 20.7 to 16.5 kcal/mol with temperature

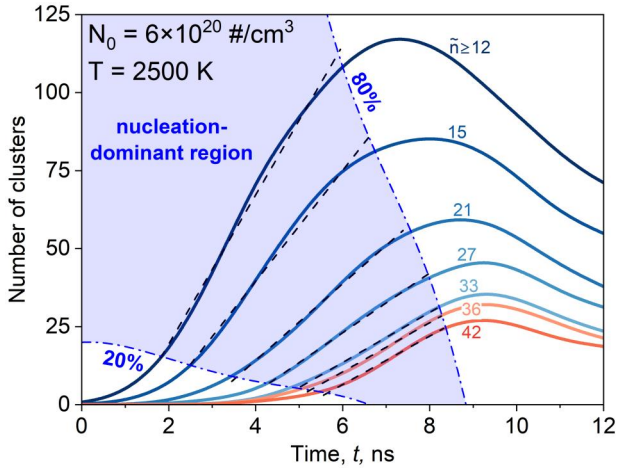

Figure 2. Temporal evolution of the number of clusters with at least $\bar{n}$ carbon atoms during pyrolysis of $N_0 = 6 \times 10^{20}$ #/cm^3 n-heptane molecules at $T = 2500$ K. The number of clusters increases monotonically regardless of the threshold cluster size $\bar{n}$ for $t \leq 7$ ns corresponding to the nucleation-dominant regime (shaded region). The nucleation-dominant region is defined as the region where the number of clusters with $n \geq \bar{n}$ ranges between 20% and 80% (dot-broken line) of their maximum number concentration (Halonen et al. 2021). For $t \geq 7.3$ ns and $\bar{n} \geq 12$, the cluster number concentration drops due to surface growth or cluster–cluster collisions. The slopes (broken lines) become almost parallel at $t = 5$–8.2 ns for $\bar{n} \geq 33$ indicating that the critical nucleus size has been reached.

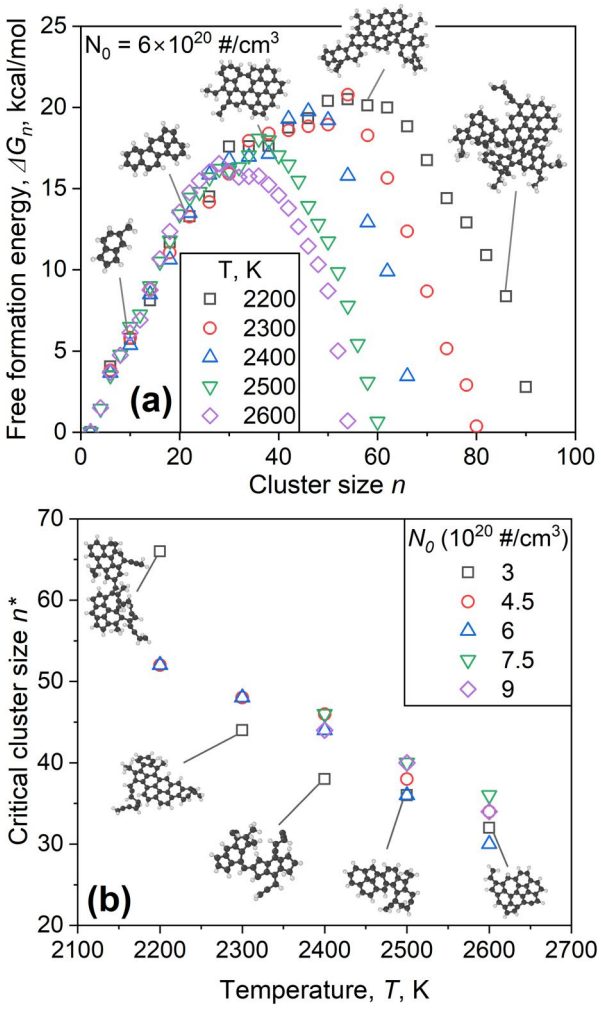

Figure 3. (a) Free energy, ΔG_n, of soot formation at steady-state nucleation as a function of the formed cluster size, n, derived by reactive MD simulations of n-heptane pyrolysis at $T = 2200$ (squares), 2300 (circles), 2400 (triangles), 2500 (inverse triangles), and 2600 K (diamonds) for $N_0 = 6 \times 10^{20}$ #/cm^3. The insets show snapshots of clusters consisting of 10, 20, 39, 61, and 87 carbon atoms formed at 2200 K. (b) Critical soot cluster size, n^*, as a function of temperature for initial n-heptane concentration $N_0 = 3$ (squares), 4.5 (circles), 6 (triangles), 7.5 (inverse triangles), and 9×10^{20} #/cm^3 (diamonds).

increasing from 2200 to 2600 K, suggesting that the clusters form more easily at higher temperatures. Lower N_0 leads to a decrease in the free formation energy barriers (e.g., Figure S7 for 2500 K), which could be associated with a diffusion-controlled process; however, the critical cluster size is hardly affected by N_0.

Figure 3b shows the critical soot cluster size, n^*, obtained by the position of the maximum $\Delta G_n{}^*$ (Figure 3a) for $N_0 = 3$ (squares), 4.5 (circles), 6 (triangles), 7.5 (inverse triangles), and 9×10^{20} #/cm^3 (diamonds) as a function of process temperature. Increasing the temperature from 2200 to 2600 K leads to almost a twofold decrease in the critical soot nucleus size, indicating the formation of thermodynamically stable clusters with fewer rings. For example, for 6×10^{20} #/cm^3, at 2200 K the critical soot nucleus consists of 52 carbon atoms while at 2600 K smaller critical nuclei of 30 carbon atoms are observed. The reduction of n^* with increasing T is consistent with the Kelvin relation for the critical diameter for particles formed by homogeneous nucleation (Friendlander 2000). Small critical clusters formed at high temperature could lead to a reduction in entropy (Blanquart and Pitsch 2007; Yu, Sumathi and Green 2004). However, the chemical complexity of these clusters, composed of branched fragments and long aliphatic side chains, may counteract this effect and increase the overall entropy. While high temperatures increase the kinetic energy of molecules, potentially leading to increased system entropy, they also promote chemical reaction kinetics and nucleation (more nucleating events per unit time), introducing competing effects that can reduce the system disorder and lower its entropy. Increasing N_0 hardly affects the critical soot cluster size (within the statistical significance of the calculation), at least for $T \geq 2300$ K. At $T = 1600 - 2000$ K, nucleation is barely

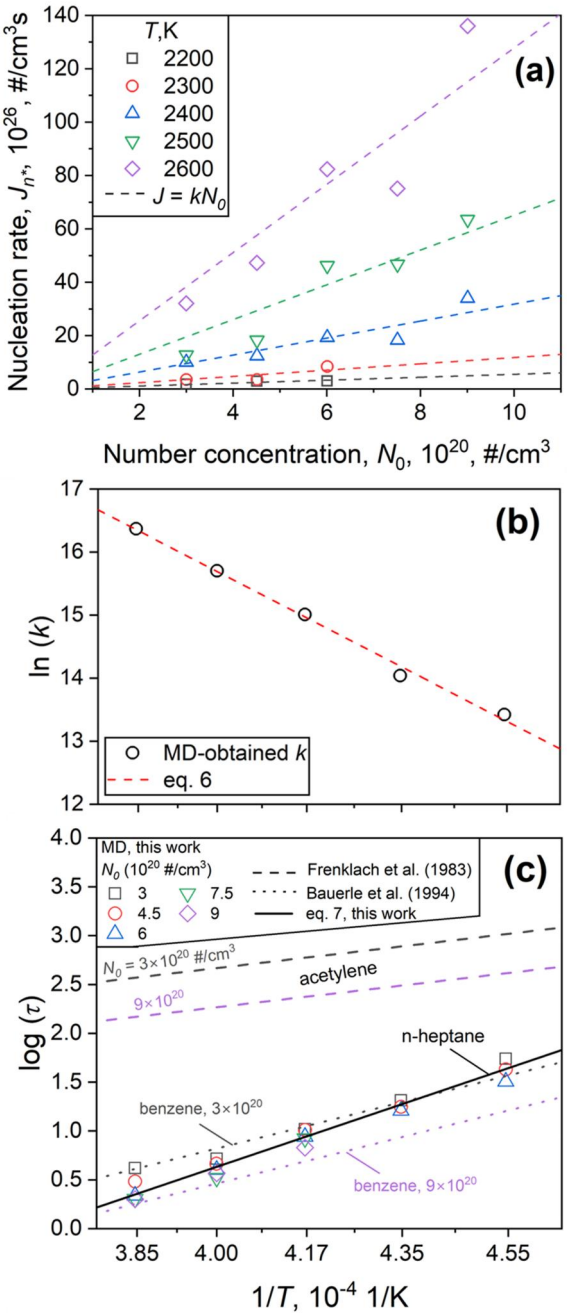

Figure 4. (a) MD-obtained nucleation rate, J_{n^*}, of incipient soot nanoparticles as a function of N_0 for n-heptane pyrolysis at $T = 2200$ (squares), 2300 (circles), 2400 (triangles), 2500 (inverse triangles), and 2600 K (diamonds). The nucleation rate increases linearly with N_0 with a slope corresponding to the nucleation rate constant, k (broken lines). (b) Arrhenius plot of ln(k) as a function of 1/T. (c) Soot induction time for pyrolysis of n-heptane obtained by MD (symbols) and Equation (7) (solid line), acetylene (broken lines) by Frenklach et al. (1983), and benzene (dotted lines) by Bauerle et al. (1994).

observed for up to 80 ns and significantly longer simulations or different techniques (e.g., accelerated MD [Hirai 2021]) might be needed.

Table 1 shows the characteristics of the MD-obtained soot critical cluster including average C/H, number of five- and six-member rings per critical cluster and aliphatic index (aliphatic/cyclic C ratio) at 2200, 2400, and 2600 K. The average C/H ratio of the critical clusters is <2, with the highest average recorded at 1.97 for 2200 K, corresponding to the largest critical cluster size. Increasing process temperature leads to decreasing fraction of five- and six-member rings per critical nucleus. For example, at 2600 K, the average number of five- and six-member rings per critical nucleus is 2.66 and 2.66, respectively, in contrast to 2200 K, where the average number of five- and six-member rings increases to 5.33 and 9.66, respectively. Interestingly, at high temperature (2400 and 2600 K), soot critical clusters have a high aliphatic index of ~0.35 due to the presence of long aliphatic side chains (e.g., blue-shaded area in Table 1). These long chains appear either as tails or bridges between "islands" of cyclic structures. At $T = 2200$ K, the critical clusters are mainly cyclic (aliphatic index ~0.05), although short bridges composed of one double bond are also observed (red-shaded area). The critical cluster structures at low temperatures resemble those observed right after the particle nucleation zone in atmospheric-pressure ethylene/air premixed laminar flames (equivalence ratio of 2.03) at $T = 1000 - 1800$ K (Schulz et al. 2019) consisting of up to 16 rings (Schulz et al. 2019: molecules M1–M10). For example, one of the largest identified molecules there, M10, has a C/H ratio of 2 and 16 rings (Schulz et al. 2019), consistent with the average C/H ratio of the MD-derived clusters reported at comparable temperatures (Table 1, $T = 2200$ K), having an average C/H ratio of 1.97 and ~15 rings.

3.2. Soot nucleation rate

Figure 4a shows the MD-obtained nucleation rate, J_{n^*}, of critical and supercritical clusters during steady-state nucleation (as discussed in Figure 2 for 6×10^{20} #/cm^3 and 2500 K) as a function of initial n-heptane number concentration at 2200–2600 K. A phenomenological model is proposed for the MD-obtained J_{n^*} with the parent fuel concentration, derived for clusters equal to or larger than the temperature-dependent critical cluster size (Figure 3). This J_{n^*} increases linearly with increasing initial n-heptane concentration N_0 for the employed temperature range following:

$$J_{n^*} = kN_0 \tag{5}$$

where k (1/s) is the nucleation rate constant. This result is consistent with semi-empirical correlations

Table 1. MD-obtained soot critical cluster characteristics including average C/H, number of rings, and aliphatic index.

T (K)	Critical size	Average C/H	Five-member ring /cluster	Six-member ring /cluster	Aliphatic index	MD-obtained critical cluster structure	AFM images and AFM-derived chemical structures (Schulz et al. 2019)
2200	52	1.97	5.33	9.66	0.05		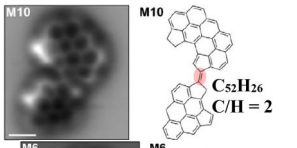
2400	44	1.38	3.33	2	0.37	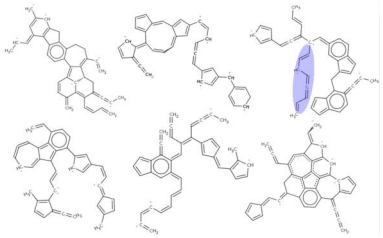	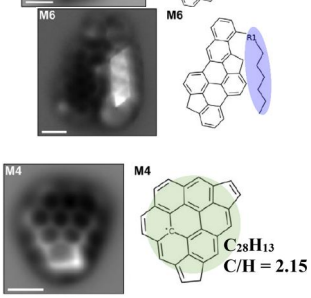
2600	30	1.55	2.66	2.66	0.32	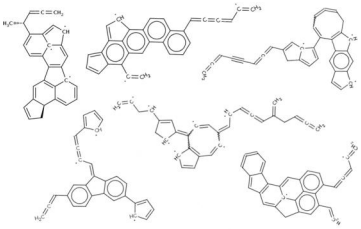	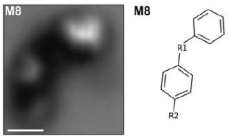

MD-obtained chemical structures, with SMILES codes generated by ChemTraYzer (Döntgen et al. 2018), are compared to those obtained by AFM (Schulz et al. 2019).
AFM: atomic force microscope; MD: molecular dynamics.

(Brookes and Moss 1999; Moss, Stewart, and Young 1995) for soot nucleation rate, proposing a first-order dependence with acetylene concentration. Figure 4b shows the Arrhenius plot of the soot nucleation rate constant obtained in Figure 4a as a function of the inverse temperature following:

$$\ln(k) = \frac{-43,190\ (\pm 1865)}{T} + 32.97\ (\pm 0.78) \qquad (6)$$

The nucleation rate increases with temperature in qualitative agreement with semi-empirical nucleation rates (Brookes and Moss 1999; Moss, Stewart, and Young 1995). The MD-obtained activation temperature of 43,190 K is in good agreement with the 46,100 K derived by Moss, Stewart, and Young (1995) based on measurements in diffusion ethylene flames.

Figure 4c shows the logarithm of the soot induction time, τ, as a function of inverse temperature for various N_0. The onset of nucleation is defined as the time that clusters larger than the critical cluster size begin to form. The effect of the threshold cluster size on the induction time is shown in Figure S8. At higher temperature the kinetic energy of the reactants increases which, in turn, promotes their chemical growth (D'Anna 2009), resulting in earlier onset of nucleation. For $T \geq 2400$ K, nucleation starts almost instantly, within $\sim$10 ns of n-heptane pyrolysis, regardless of N_0. At lower temperature ($T \leq 2300$ K), however, the onset of nucleation is delayed, as even large cyclic molecules ($n \leq 52$) are subcritical and prone to dissociation (Figure 3a). The MD-derived induction time decreases exponentially with temperature:

$$\tau(ns) = 10^{-6.72}\ e^{(42320/T(K))} \qquad (7)$$

exhibiting a similar trend with fitted correlations from shock tube pyrolysis experiments for benzene (Bauerle et al. 1994) (dotted lines), extrapolated for the N_0 range employed here. Much longer induction times are observed for acetylene (Frenklach et al. 1983) (broken lines), attributed to its smaller molecular weight compared to n-heptane, as decomposition of large organic molecules results in smaller reactive species with high number density, promoting faster nucleation. In addition, the measurement error by light extinction can underestimate the incipient soot

volume fraction and, thus, overestimate the induction time, compounded by the detection limit of instruments being higher than the cluster sizes tracked by MD. The empirical correlation for acetylene induction time was developed (Frenklach et al. 1983) for a pressure range of 0.3–7 bar, which is ~7–20 times lower than the pressures considered here. An increase in the fuel concentration from 3×10^{20} to $9 \times 10^{20}\,m^{-3}$ results in 39% faster nucleation in MD, consistent with empirical models for benzene (Bauerle et al. 1994) and acetylene (Frenklach et al. 1983), predicting 56% and 60% shorter induction times, respectively (Figure 4c). Direct comparison of MD and experimental data is shown in Figure S9, even though no measurements are available for soot induction by n-heptane.

Equation (7) is in line with previous MD results (Mao, van Duin, and Luo 2017), suggesting that no nucleation occurs at 1600–2400 K within the first 2 ns of A2–A10 PAH pyrolysis. However, caution is needed in determining the occurrence of chemical nucleation, especially at intermediate temperatures, as long times might be required for the onset of nucleation. Here, the induction time is defined as the onset of formation of the first one to two critical clusters from initially 1000 n-heptane molecules (equivalent to 7000 carbon atoms). While this system size is sufficient for observing nucleation events, larger system sizes (e.g., 64,000 molecules [Song, Berry, and Goudeli 2023]) can provide greater statistical significance.

It should be noted that the high temperature and high pressure conditions employed in the present MD, make Equations (6) and (7) relevant to high fuel-rich environments. A systematic investigation of the effect of oxygen on soot nucleation is required for the oxygen-rich phases of the gasoline engine cycle, since soot formation is highly dependent on combustion conditions and oxygen concentrations, as demonstrated by soot volume fraction measurements in ethylene combustion (Mei et al. 2021) and n-heptane counterflow diffusion flames (Zheng et al. 2023).

3.3. Comparison with kinetic modeling

Figure 5a shows the temporal evolution of the number density of n-heptane molecules with $N_0 = 3 \times 10^{20}$ #/cm^3, during pyrolysis at 2500 K, obtained by MD simulations (dotted line) and kinetic modeling (solid line) of soot nucleation. The MD-derived dissociation rate of n-heptane decreases with time logarithmically, in agreement with kinetic modeling predictions using a well-established reaction mechanism (Blanquart, Pepiot-Desjardins, and Pitsch 2009), validating the present simulations for the pressure and temperature ranges used here. The decomposition rate of n-heptane is also in agreement with that predicted by the KAUST mechanism (Raj et al. 2012) (Figure S10: broken line), developed for gasoline surrogate fuels like n-heptane. The good agreement between MD and kinetic modeling in Figure 5a validates the n-heptane chemistry in this mechanism, but not necessarily the sub-models for the large PAH chemistry. Validating PAH chemistry remains challenging, as tracking the evolution of various PAHs in MD simulations is difficult due to species identification limitations.

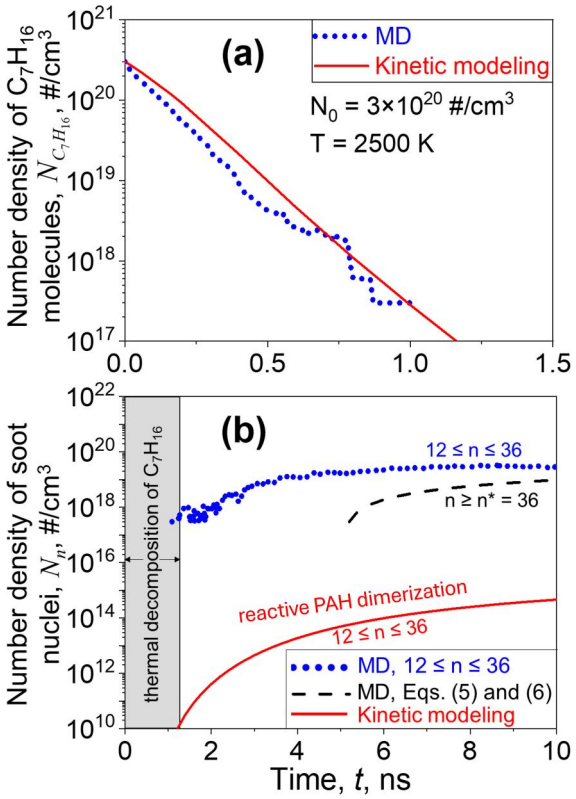

Figure 5. Temporal evolution of the number of (a) n-heptane molecules and (b) clusters with $12 \leq \bar{n} \leq 36$ obtained by MD (dotted line), Equations (5) and (6) (broken line), and by kinetic modeling (solid line) during pyrolysis at 2500 K and $N_0 = 3 \times 10^{20}$ #/cm^3.

Figure 5b shows soot N_n obtained by MD for clusters with $n \geq n^* = 36$ (Equations (5) and (6); broken line), as well as with $n = 12$–36 (dotted line) to be consistent with the n range used in kinetic modeling (solid line). Soot N_n derived by Equations (5) and (6) for $n \geq n^* = 36$ (broken lines) starts to increase at about 5 ns and reaches a value of 9.43×10^{18} #/cm^3 at 10 ns. Accounting for soot nuclei with $n = 12$–36 results in earlier N_n increase at 1.2 ns, which approaches 2.88×10^{19} #/cm^3 at 10 ns, three times

higher than the density estimated for $n \geq n^* = 36$, as expected. The soot N_n derived by kinetic modeling for reactive dimerization of benzene (A1) to cyclopenta-[cd]-pyrene (A4R5) PAHs (Section 2.4) (Kholghy, Kelesidis, and Pratsinis 2018) exhibits a similar a trend to the MD-obtained evolutions but is four to five orders of magnitude lower than the MD-predicted soot N_n, regardless of the cluster sizes considered. The pressure profile obtained from kinetic modeling is in excellent agreement with that obtained by MD (Figure S11). This large discrepancy can be attributed partly to the distinct dimer combinations (e.g., A1 + A1, A1 + A2, A1 + A3, A4R5+ A4R5) accounted for by kinetic modeling that do not include all potential molecule sizes and combinations (or the large chemical reactions network) that are accounted for intrinsically in MD. For example, high temperatures promote the formation of polyynes, which may result from the breakdown of ring structures rather than PAH dimerization (Krestinin 1998). These structures may form in MD (e.g., Table 1, $T = 2600$ K) and, hence, are accounted for in the MD-obtained nucleation rate, in contrast to the soot nucleation kinetic mechanism that does not account for polyyne condensation. Extrapolation of PAH chemistry beyond its validated temperature range may contribute to the underprediction of soot nucleation in kinetic modeling. So, the semi-empirical model for reactive dimerization of PAHs (Kholghy, Kelesidis, and Pratsinis 2018) might significantly underestimate the nucleation rate of soot. This may explain the underestimation of the measured soot volume fraction by this kinetic model in diffusion ethylene flames (Kholghy et al. 2019; Figure 4a).

4. Conclusions

Chemical nucleation of carbon-based nanoparticles during high-pressure n-heptane pyrolysis is investigated by reactive MD at 2200–2600 K. The free formation energy of carbonaceous clusters is used to quantify the critical nucleus size. The nucleus size drops from 59 ± 7 carbon atoms at 2200 K down to 33 ± 3 carbons atoms at 2600 K, indicating the formation of thermodynamically stable clusters with fewer rings at higher temperature. However, the initial fuel concentration hardly affects the critical size for $3 \times 10^{20} - 9 \times 10^{20}$ #/cm^3. The nucleation rate is determined by tracking the rate of formation of critical and supercritical clusters. An equation for the nucleation rate is proposed by MD, for the first time to our knowledge, revealing a first-order dependency with initial fuel concentration. The MD-derived n-heptane consumption rate by pyrolysis is in agreement with kinetic modeling based on nucleation by reactive PAH dimerization. However, the number density of soot nuclei predicted by the MD-derived nucleation rate is four to five orders of magnitude larger than that obtained by the kinetic modeling based on nucleation by reactive PAH dimerization. The proposed easy-to-use nucleation rate can be readily applied in particle dynamic models for large and complex geometries, without the need to rely on detailed chemical reaction kinetic modeling for soot nucleation, which depends on individual reaction rate constants and demand significant computational resources.

Author contributions

CRediT: **Arash Karharnezhad**: Conceptualization, Methodology, Software, Formal analysis (MD), Writing–review & editing; **Dimitri M. Saad**: Software, Formal analysis (kinetic modeling); **Georgios A. Kelesidis**: Supervision (kinetic modeling), Writing–review & editing; **Eirini Goudeli**: Supervision, Conceptualization, Writing–review & editing, Methodology, Project administration, Resources.

Disclosure statement

No potential conflict of interest was reported by the author(s).

Funding

This work was supported by the University of Melbourne Computing Services and a National Computational Infrastructure (NCI) high-performance compute time grant under the National Computational Merit Allocation Scheme (NCMAS).

Supplemental information

Figures showing fraction of radicals, free formation energy, soot induction time, temporal evolutions of number of molecules, radicals and rings, and a table with detailed nucleation rate and critical cluster size values.

ORCID

Arash Fakharnezhad http://orcid.org/0000-0002-7703-4239

References

An, Y. Z., S. P. Teng, Y. Q. Pei, J. Qin, X. Li, and H. Zhao. 2016. An experimental study of polycyclic aromatic hydrocarbons and soot emissions from a GDI engine

fueled with commercial gasoline. *Fuel* 164:160–71. doi: 10.1016/j.fuel.2015.10.007.

Ashraf, C., and A. C. van Duin. 2017. Extension of the ReaxFF combustion force field toward syngas combustion and initial oxidation kinetics. *J. Phys. Chem. A* 121 (5): 1051–68. doi: 10.1021/acs.jpca.6b12429.

Bauerle, S., Y. Karasevich, S. Slavov, D. Tanke, M. Tappe, T. Thienel, and H. G. Wagner. 1994. Soot formation at elevated pressures and carbon concentrations in hydrocarbon pyrolysis. *Symp. Combust. Proc.* 25:627–34. doi: 10.1016/s0082-0784(06)80694-6.

Blanquart, G., P. Pepiot-Desjardins, and H. Pitsch. 2009. Chemical mechanism for high temperature combustion of engine relevant fuels with emphasis on soot precursors. *Combust. Flame* 156 (3):588–607. doi: 10.1016/j.combustflame.2008.12.007.

Blanquart, G., and H. Pitsch. 2007. Thermochemical properties of polycyclic aromatic hydrocarbons (PAH) from G3MP2B3 calculations. *J. Phys. Chem. A* 111 (28):6510–20. doi: 10.1021/jp068579w.

Bond, T. C., S. J. Doherty, D. W. Fahey, P. M. Forster, T. Berntsen, B. J. DeAngelo, M. G. Flanner, S. Ghan, B. Kärcher, D. Koch, et al. 2013. Bounding the role of black carbon in the climate system: A scientific assessment. *J. Geophys. Res. Atmos.* 118 (11):5380–552. doi: 10.1002/jgrd.50171.

Brookes, S. J., and J. B. Moss. 1999. Predictions of soot and thermal radiation properties in confined turbulent jet diffusion flames. *Combust. Flame* 116 (4):486–503. doi: 10.1016/S0010-2180(98)00056-X.

Chu, Q., C. Wang, and D. Chen. 2022. Toward full *ab initio* modeling of soot formation in a nanoreactor. *Carbon* 199:87–95. doi: 10.1016/j.carbon.2022.07.055.

D'Anna, A. 2009. Combustion-formed nanoparticles. *Proc. Combust. Inst.* 32 (1):593–613. doi: 10.1016/j.proci.2008.09.005.

Desgroux, P., A. Faccinetto, X. Mercier, T. Mouton, D. A. Karkar, and A. El Bakali. 2017. Comparative study of the soot formation process in a "nucleation" and a "sooting" low pressure premixed methane flame. *Combust. Flame* 184:153–66. doi: 10.1016/j.combustflame.2017.05.034.

Diemand, J., R. Angélil, K. K. Tanaka, and H. Tanaka. 2013. Large scale molecular dynamics simulations of homogeneous nucleation. *J. Chem. Phys.* 139 (7):074309. doi: 10.1063/1.4818639.

Ding, J., L. Zhang, Y. Zhang, and K. L. Han. 2013. A reactive molecular dynamics study of n-heptane pyrolysis at high temperature. *J. Phys. Chem. A* 117 (16):3266–78. doi: 10.1021/jp311498u.

Döntgen, M., F. Schmalz, W. A. Kopp, L. C. Kröger, and K. Leonhard. 2018. Automated chemical kinetic modeling via hybrid reactive molecular dynamics and quantum chemistry simulations. *J. Chem. Inf. Model.* 58 (7):1343–55. doi: 10.1021/acs.jcim.8b00078.

Frenklach, M. 2002. Reaction mechanism of soot formation in flames. *Phys. Chem. Chem. Phys.* 4 (11):2028–37. doi: 10.1039/b110045a.

Frenklach, M., and A. M. Mebel. 2020. On the mechanism of soot nucleation. *Phys. Chem. Chem. Phys.* 22 (9):5314–31. doi: 10.1039/d0cp00116c.

Frenklach, M., S. Taki, M. B. Durgaprasad, and R. A. Matula. 1983. Soot formation in shock-tube pyrolysis of acetylene, allene, and 1,3-butadiene. *Combust. Flame* 54 (1–3):81–101. doi: 10.1016/0010-2180(83)90024-X.

Frenklach, M., and H. Wang. 1991. Detailed modeling of soot particle nucleation and growth. *Symp. Combust. Proc.* 23 (1):1559–66. doi: 10.1016/s0082-0784(06)80426-1.

Frenklach, M., and H. Wang. 1994. Detailed mechanism and modeling of soot particle formation. In *Soot formation in combustion*, 165–92. Berlin, Heidelberg: Springer.

Friendlander, S. 2000. *Smoke, dust and haze: Fundamentals of aerosol dynamics*. New York: Oxford University Press.

Gentile, F. S., F. Picca, G. De Falco, M. Commodo, P. Minutolo, M. Causà, and A. D'Anna. 2020. Soot inception: A DFT study of σ and π dimerization of resonantly stabilized aromatic radicals. *Fuel* 279:118491. doi: 10.1016/j.fuel.2020.118491.

Gilyazetdinov, L. 1972. The kinetic and formation mechanism of carbon black during thermo decomposition of hydrocarbons in the gas phase. *Khim. Tverd. Topl.* 3:103.

Gleason, K., F. Carbone, A. J. Sumner, B. D. Drollette, D. L. Plata, and A. Gomez. 2021. Small aromatic hydrocarbons control the onset of soot nucleation. *Combust. Flame* 223: 398–406. doi: 10.1016/j.combustflame.2020.08.029.

Halonen, R. 2022. Comments on "The proper view of cluster free energy in nucleation theories" by Runlong Cai and Juha Kangasluoma. *Aerosol Sci. Technol.* 56 (11): 976–9. doi: 10.1080/02786826.2022.2114310.

Halonen, R., V. Tikkanen, B. Reischl, K. K. Dingilian, B. E. Wyslouzil, and H. Vehkamäki. 2021. Homogeneous nucleation of carbon dioxide in supersonic nozzles ii: Molecular dynamics simulations and properties of nucleating clusters. *Phys. Chem. Chem. Phys.* 23 (8):4517–29. doi: 10.1039/d0cp05653g.

Harris, S. J., and A. M. Weiner. 1985. Chemical-kinetics of soot particle growth. *Annu. Rev. Phys. Chem.* 36 (1):31–52. doi: 10.1146/annurev.physchem.36.1.31.

Hirai, H. 2021. Molecular dynamics simulations for initial formation process of polycyclic aromatic hydrocarbons in n-hexane and cyclohexane combustion. *Chem. Phys.* 548: 111225. doi: 10.1016/j.chemphys.2021.111225.

Hu, J., S. Zhong, and T. Yan. 2021. Using carbon black to facilitate fast charging in lithium-ion batteries. *J. Power Sources* 508:230342. doi: 10.1016/j.jpowsour.2021.230342.

International Carbon Black Association. 2016. Carbon black user's guide: Safety, health, & environmental information. https://www.carbon-black.org/.

Jerrett, M., R. T. Burnett, B. S. Beckerman, M. C. Turner, D. Krewski, G. Thurston, R. V. Martin, A. van Donkelaar, E. Hughes, Y. Shi, 3rd., et al. 2013. Spatial analysis of air pollution and mortality in California. *Am. J. Respir. Crit. Care Med.* 188 (5):593–9. doi: 10.1164/rccm.201303-0609OC.

Johansson, K. O., M. P. Head-Gordon, P. E. Schrader, K. R. Wilson, and H. A. Michelsen. 2018. Resonance-stabilized hydrocarbon-radical chain reactions may explain soot inception and growth. *Science* 361 (6406):997–1000. doi: 10.1126/science.aat3417.

Kee, R. J., F. M. Rupley, and J. A. Miller. 1989. *Chemkin-ii: A Fortran chemical kinetics package for the analysis of gas-phase chemical kinetics.* Livermore, CA: Sandia National Lab (SNL-CA).

Kennedy, I. M. 1997. Models of soot formation and oxidation. *Prog. Energy Combust. Sci.* 23 (2):95–132. doi: 10.1016/S0360-1285(97)00007-5.

Kholghy, M. R., N. A. Eaves, A. Veshkini, and M. J. Thomson. 2019. The role of reactive PAH dimerization in reducing soot nucleation reversibility. *Proc. Combust. Inst.* 37 (1):1003–11. doi: 10.1016/j.proci.2018.07.110.

Kholghy, M. R., G. A. Kelesidis, and S. E. Pratsinis. 2018. Reactive polycyclic aromatic hydrocarbon dimerization drives soot nucleation. *Phys. Chem. Chem. Phys.* 20 (16): 10926–38. doi: 10.1039/C7CP07803J.

Kleiveland, R. N. 2005. Modelling of soot formation and oxidation in turbulent diffusion flames. Doctoral thesis, NTNU, Trondheim, Norway.

Kohse-Höinghaus, K. 2020. Combustion in the future: The importance of chemistry. *Proc. Combust. Inst.* 38 (1): 1–56. doi: 10.1016/j.proci.2020.06.375.

Krestinin, A. V. 1998. Polyyne model of soot formation process. *Symp. Combust. Proc.* 27 (1):1557–63. doi: 10.1016/S0082-0784(98)80564-X.

Leung, K. M., R. P. Lindstedt, and W. P. Jones. 1991. A simplified reaction-mechanism for soot formation in nonpremixed flames. *Combust. Flame* 87 (3–4):289–305. doi: 10.1016/0010-2180(91)90114-Q.

Li, D. D., C. Wang, Q. N. Chan, and G. H. Yeoh. 2023. Soot: A review of computational models at different length scales. *Exp. Comput. Multiph. Flow* 5 (1):1–14. doi: 10.1007/s42757-021-0124-4.

Lindstedt, P. R. 1994. Simplified soot nucleation and surface growth steps for non-premixed flames. In *Soot formation in combustion: Mechanisms and models*, 417–41. Berlin, Heidelberg: Springer.

Ma, C., L. Wu, M. Dirican, H. Cheng, J. Li, Y. Song, J. Shi, and X. Zhang. 2021. Carbon black-based porous submicron carbon fibers for flexible supercapacitors. *Appl. Surf. Sci.* 537:147914. doi: 10.1016/j.apsusc.2020.147914.

Mao, Q., A. C. T. van Duin, and K. H. Luo. 2017. Formation of incipient soot particles from polycyclic aromatic hydrocarbons: A ReaxFF molecular dynamics study. *Carbon* 121: 380–8. doi: 10.1016/j.carbon.2017.06.009.

Martin, J. W., D. Hou, A. Menon, L. Pascazio, J. Akroyd, X. You, and M. Kraft. 2019. Reactivity of polycyclic aromatic hydrocarbon soot precursors: Implications of localized π-radicals on rim-based pentagonal rings. *J. Phys. Chem. C* 123 (43):26673–82. doi: 10.1021/acs.jpcc.9b07558.

Martin, J. W., M. Salamanca, and M. Kraft. 2022. Soot inception: Carbonaceous nanoparticle formation in flames. *Prog. Energy Combust. Sci.* 88:100956. doi: 10.1016/j.pecs.2021.100956.

Mei, J., Y. Zhou, X. You, and C. K. Law. 2021. Formation of nascent soot during very fuel-rich oxidation of ethylene at low temperatures. *Combust. Flame* 226:31–41. doi: 10.1016/j.combustflame.2020.11.031.

Menon, A., J. W. Martin, J. Akroyd, and M. Kraft. 2020. Reactivity of polycyclic aromatic hydrocarbon soot precursors: Kinetics and equilibria. *J. Phys. Chem. A* 124 (48):10040–52. doi: 10.1021/acs.jpca.0c07811.

Miller, J. H. 2005. Aromatic excimers: Evidence for polynuclear aromatic hydrocarbon condensation in flames. Proc. Combust. Inst. 30:1381–8. doi: 10.1016/j.proci.2004.08.192.

Moss, J. B., C. D. Stewart, and K. J. Young. 1995. Modeling soot formation and burnout in a high-temperature laminar diffusion flame burning under oxygen-enriched conditions. *Combust. Flame* 101 (4):491–500. doi: 10.1016/0010-2180(94)00233-I.

Plimpton, S. 1995. Fast parallel algorithms for short-range molecular-dynamics. *Comput. Phys.* 117 (1):1–19. doi: 10.1006/jcph.1995.1039.

Raj, A., I. D. C. Prada, A. A. Amer, and S. H. Chung. 2012. A reaction mechanism for gasoline surrogate fuels for large polycyclic aromatic hydrocarbons. *Combust. Flame* 159 (2):500–15. doi: 10.1016/j.combustflame.2011.08.011.

Raj, A., M. Sander, V. Janardhanan, and M. Kraft. 2010. A study on the coagulation of polycyclic aromatic hydrocarbon clusters to determine their collision efficiency. *Combust. Flame* 157 (3):523–34. doi: 10.1016/j.combustflame.2009.10.003.

Sabbah, H., L. Biennier, S. J. Klippenstein, I. R. Sims, and B. R. Rowe. 2010. Exploring the role of PAHs in the formation of soot: Pyrene dimerization. *J. Phys. Chem. Lett.* 1 (19):2962–7. doi: 10.1021/jz101033t.

Schmalz, F., W. A. Kopp, E. Goudeli, and K. Leonhard. 2024. Reaction path identification and validation from molecular dynamics simulations of hydrocarbon pyrolysis. *Int. J. Chem. Kinet.* 56 (9):501–12. doi: 10.1002/kin.21719.

Schuetz, C. A., and M. Frenklach. 2002. Nucleation of soot: Molecular dynamics simulations of pyrene dimerization. *Proc. Combust. Inst.* 29 (2):2307–14. doi: 10.1016/S1540-7489(02)80281-4.

Schulz, F., M. Commodo, K. Kaiser, G. De Falco, P. Minutolo, G. Meyer, A. D′Anna, and L. Gross. 2019. Insights into incipient soot formation by atomic force microscopy. *Proc. Combust. Inst.* 37 (1):885–92. doi: 10.1016/j.proci.2018.06.100.

Scienomics. 2020. *Maps Platform*, *4.4*, Paris, France. http://www.scienomics.com/.

Sharma, A., K. M. Mukut, S. P. Roy, and E. Goudeli. 2021. The coalescence of incipient soot clusters. *Carbon* 180: 215–25. doi: 10.1016/j.carbon.2021.04.065.

Siegmann, K., K. Sattler, and H. C. Siegmann. 2002. Clustering at high temperatures: Carbon formation in combustion. *J. Electron Spectrosc. Relat. Phenom.* 126 (1–3):191–202. doi: 10.1016/S0368-2048(02)00152-4.

Smith, C. J., P. M. Forster, M. Allen, J. Fuglestvedt, R. J. Millar, J. Rogelj, and K. Zickfeld. 2019. Current fossil fuel infrastructure does not yet commit us to 1.5°C warming. *Nat. Commun.* 10 (1):101. doi: 10.1038/s41467-018-07999-w.

Song, J., J. D. Berry, and E. Goudeli. 2023. Nucleation rate of N_2 and O_2 in cryogenic H_2 and He. *J. Phys. Chem. B* 127 (46):9976–84. doi: 10.1021/acs.jpcb.3c03364.

Stiesch, G. 2003. *Modeling engine spray and combustion processes*. Berlin Heidelberg: Springer.

Tanelli, C., and S. Maranta. 2015. Modeling soot emissions in diesel engines by means of semi-empirical approaches and a combustion model based on detailed chemistry, Doctoral thesis, Politecnico di Milano, Milan, Italy.

Veshkini, A., N. A. Eaves, S. B. Dworkin, and M. J. Thomson. 2016. Application of PAH-condensation reversibility in modeling soot growth in laminar premixed and nonpremixed flames. *Combust. Flame* 167: 335–52. doi: 10.1016/j.combustflame.2016.02.024.

Wang, H. 2011. Formation of nascent soot and other condensed-phase materials in flames. *Proc. Combust. Inst.* 33 (1):41–67. doi: 10.1016/j.proci.2010.09.009.

Yasuoka, K., and M. Matsumoto. 1998. Molecular dynamics of homogeneous nucleation in the vapor phase. I. Lennard-Jones fluid. *J. Chem. Phys.* 109 (19):8451–62. doi: 10.1063/1.477509.

Yu, J., R. Sumathi, and W. H. Green. 2004. Accurate and efficient method for predicting thermochemistry of polycyclic aromatic hydrocarbons – Bond-centered group additivity. *J. Am. Chem. Soc.* 126 (39):12685–700. doi. doi: 10.1021/ja048333+.

Yuan, T., L. Zhang, Z. Zhou, M. Xie, L. Ye, and F. Qi. 2011. Pyrolysis of n-heptane: Experimental and theoretical study. *J. Phys. Chem. A* 115 (9):1593–601. doi: 10.1021/jp109640z.

Zheng, D., A. Nobili, A. Cuoci, M. Pelucchi, X. Hui, and T. Faravelli. 2023. Soot formation from n-heptane counterflow diffusion flames: Two-dimensional and oxygen effects. *Combust. Flame* 258:112441. doi: 10.1016/j.combustflame.2022.112441.